

# Modelling temperature-dependent dynamics of single and mixed infections in a plant virus



Josep Sardanyés<sup>a,b,\*</sup>, Cristina Alcaide<sup>c</sup>, Pedro Gómez<sup>c</sup>, Santiago F. Elena<sup>d,e</sup>

<sup>a</sup> Centre de Recerca Matemàtica (CRM). Edifici C, Campus de Bellaterra, 08193 Cerdanyola del Vallès, Barcelona, Spain

<sup>b</sup> Dynamical Systems and Computational Virology, CSIC Associated Unit CRM-Institute for Integrative Systems Biology (I<sup>2</sup>SysBio), Spain

<sup>c</sup> Centro de Edafología y Biología Aplicada del Segura (CEBAS), CSIC, Departamento de Biología del Estrés y Patología Vegetal, PO Box 164, 30100, Murcia, Spain

<sup>d</sup> I<sup>2</sup>SysBio, CSIC-Universitat de València, Parc Científic UV, Paterna 46182 València, Spain

<sup>e</sup> Santa Fe Institute, 1399 Hyde Park Road, Santa Fe, NM 87501, USA

## ARTICLE INFO

### Article history:

Received 4 June 2021

Revised 1 October 2021

Accepted 4 October 2021

Available online 13 October 2021

### Keywords:

Abiotic stress

Bifurcations

Co-infection dynamics

Dynamical systems

Nonlinear dynamics

Thermal reaction norms

Transcritical bifurcations

## ABSTRACT

Multiple viral infection is an important issue in health and agriculture with strong impacts on society and the economy. Several investigations have dealt with the population dynamics of viruses with different dynamic properties, focusing on strain competition during multiple infections and the effects on viruses' hosts. Recent interest has been on how multiple infections respond to abiotic factors such as temperature ( $T$ ). This is especially important in the case of plant pathogens, whose dynamics could be affected significantly by global warming. However, few mathematical models incorporate the effect of  $T$  on parasite fitness, especially in mixed infections. Here, we investigate simple mathematical models incorporating thermal reaction norms (TRNs), which allow for quantitative analysis. A logistic model is considered for single infections, which is extended to a Lotka-Volterra competition model for mixed infections. The dynamics of these two models are investigated, focusing on the roles of  $T$ -dependent replication and competitive interactions in both transient and asymptotic dynamics. We determine the scenarios of co-existence and competitive exclusion, which are separated by a transcritical bifurcation. To illustrate the applicability of these models, we ran single- and mixed-infection experiments in plants growing at 20 °C and 30 °C using two strains of the plant RNA virus *Pepino mosaic virus*. Using a macroevolutionary algorithm, we fitted the models to the data by estimating the TRNs for both strains in single infections. Then, we used these TRNs to feed the mixed-infection model estimating the strength of competition. We found an asymmetrical pattern in which each strain dominated at different  $T$  values due to differences in their TRNs. We also identified that  $T$  can modify competition interference greatly for both isolates. The models proposed here can be useful for investigating the outcomes of multiple-infection dynamics under abiotic changes and have implications for the understanding of viral responses to global warming.

© 2021 The Author(s). Published by Elsevier Inc.

This is an open access article under the CC BY-NC-ND license

(<http://creativecommons.org/licenses/by-nc-nd/4.0/>)

\* Corresponding author.

E-mail address: [jsardanyes@crm.cat](mailto:jsardanyes@crm.cat) (J. Sardanyés).

## 1. Introduction

Many examples exist of different parasites infecting a host simultaneously [1,2]. This is of special importance because multiple infection can cause huge impacts on health and agriculture, thus having severe ecological and socio-economic consequences [3,4]. Regarding diseases impacting human health, human immunodeficiency virus type-1 (HIV-1) [5,6] can coinfect with tuberculosis (TB) [7], the hepatitis B [8,9] and C viruses [10], and malaria [11]. Other common examples of multiple infection include infection by the hepatitis B and C viruses [12], gonorrhea and chlamydia [13], and herpes simplex viruses 1 and 2 [14,15]. In all cases, the outcomes of multiple infection differ from the observed from the single infection cases. The dynamics of different pathogenic microbial strains infecting the same host mainly have been studied with dynamical systems theory such as for general diseases [16–19] and microparasites (viruses, bacteria, protozoa, or fungi) [20–28]. More recently, several studies have focused on the dynamical outcomes of different evolving virus strains with different infectious phenotypes, i.e., specialist vs. generalist, infecting host cells [29,30]. Multiple infection dynamics, in the form of both coinfections and superinfections, have also been an object of intense mathematical modeling [22,23].

Mixed viral infection is especially relevant for plant crops [2,31–34]. In this sense, within-plant virus–virus interactions can affect a plant's epidemiology as a result of synergistic or antagonistic interactions among infecting strains [33] or viral species [2]. They also have major consequences on virulence and virus fitness [34–37]. Emerging plant viruses are responsible for widespread crops epidemics, representing a major challenge to plant health and thus to agriculture [38–40]. This emergence has driven by intrinsic viral and host factors, in addition to ecological, agronomic and socio-economic factors [41–44]. An important yet poorly explored issue is how environmental abiotic stresses such as droughtiness, salinity, light intensity, and temperature alter plant physiology and thus affect coinfecting viruses at the within-host scale. This becomes an important question given the ongoing global warming scenario [45]. Climate change is likely to increase the frequency of viral diseases emerging in plant crops [46–48]. Warming and highly variable climate may directly and indirectly affect host, vectors, and viral traits, further influencing viral epidemics in both wild and cultivated plants. Therefore, exploring how and to what extent temperature variations may affect the eco-evolutionary dynamics of viral populations can contribute to a more complete understanding of how global warming will affect virus emergence and epidemiology.

Typically, multi-strain mathematical models use different fitness traits, e.g., replication capacity, to determine how competitive interactions affect transients and equilibrium dynamics [25–30,49]. However, as mentioned above, the successful replication and infection of these pathogens may also depend on environmental abiotic factors. That is, different strains may have different responses to such environmental components of the ecosystem.

In this article, we introduce and investigate mathematical dynamical models explicitly considering temperature ( $T$ )-dependent replication. We do so by considering the so-called thermal reaction norm (TRN). Briefly, reaction norms relate fitness with some environmental variable: the TRN describes how a particular virus strain responds to different temperatures. The model for single infections considers a time-continuous logistic model, which describes exponential replication (at small population values) and includes intra-specific competition, together with the  $T$ -dependent replication. This simple model is extended to a Lotka–Volterra competition model with two strains. The dynamics of these models are investigated analytically and numerically, focusing on the role of  $T$ -dependent replication. The two viruses competition model reveals a transition between coexistence and out-competition through a transcritical bifurcation. As a practical application, we finally use these models to fit experimental data gathered for *Pepino mosaic virus* (PepMV; genus *Potexvirus*, family *Alphaflexiviridae*) strains infecting tomato plants at 20 °C and 30 °C, considering both single and mixed infections (see also [50]).

PepMV has a major impact on tomato production worldwide. PepMV populations mainly comprise a mixture of two types of co-circulating isolates: the European (EU) and Chilean (CH2) strains [51]. The CH2 type isolates are predominant. However, EU isolates have not been displaced but persist mainly in mixed infections. The CH2 strain has higher fitness than the EU strain does [51]; hence, the question remaining to be answered is what mechanisms may promote coexistence, despite this fitness advantage of the CH2 strain. Our model for mixed infection confirms the stable coexistence of both strains under different fitness values, while also allowing both the TRNs and competition coefficients to be quantified.

## 2. Mathematical models

In the next sections, we introduce and analyze the mathematical models for single and mixed infection at different temperatures ( $T$ ). The models assume well-mixed viral populations and are aimed at describing within-host (*in planta*) virus replication. As mentioned at the end of the Introduction section, we used a logistic time-continuous model for single infection, including a  $T$ -dependent replication (fitness) parameter. We will refer to the viral load with the variable  $x_i$ . Because the experimental results were obtained using the EU and CH2 strains, we will hereafter use subindices  $E$  and  $C$  to represent them, respectively.

### 2.1. Modelling the effect of temperature in virus replication

In this section, we introduce the function used to model  $T$ -dependent replication rates,  $r_i(T)$  with  $i \in \{E, C\}$ , i.e., the TRN. This function (see [52–54] for details) reads as follows:

$$r_i(T) = a_i(T - T_{min}) \left[ 1 - \exp(b_i(T - T_{max})) \right]. \quad (1)$$

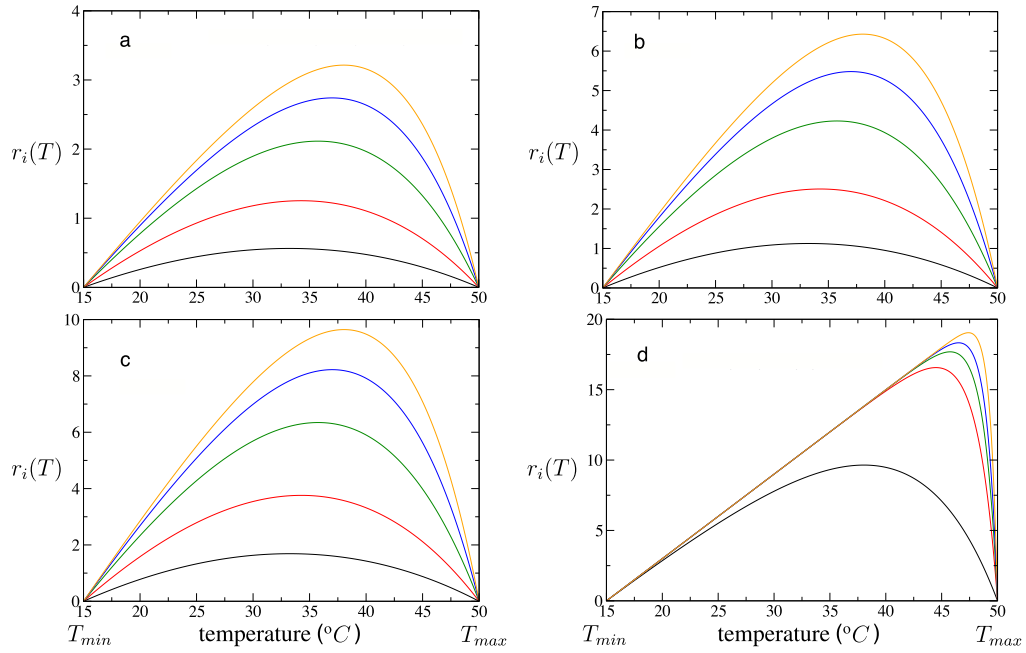


**Fig. 1.** Thermal reaction norms modeled by Eq. (1), which provide replication rates,  $r_i(T)$ , as a function of temperature. We show results for  $a_i = 0.2$  (a),  $a_i = 0.4$  (b), and  $a_i = 0.6$  (c), using different values of  $b_i$ : 0.010 (black), 0.025 (red), 0.050 (green), 0.075 (blue), and 0.100 (orange). Panel (d) was computed by setting  $a_i = 0.6$  and using larger values of  $b_i$ : 0.10 (black), 0.50 (red), 0.75 (green), 1.00 (blue), and 1.50 (orange).

Equation (1) is a bell-shaped function assuming that the PepMV genome's (gRNA) replication response to  $T$  is nonlinear, increasing as  $T$  grows until reaching an optimal  $T$  for replication. These nonlinear thermal traits have improved the predictions for several diseases (see [45] for a review). Parameters  $a_i$  and  $b_i$  allow the bell's height and shape to be tuned. As our first approach,  $a_i$  mainly determined the magnitude of the optimal  $T$  while  $b_i$  defined the asymmetry of the TRN, thus influencing the location of the optimal  $T$ . In our analyses, we set the range of temperatures between  $T_{\min} = 15^\circ\text{C} \leq T \leq 50^\circ\text{C} = T_{\max}$ . To illustrate the behavior of Eq. (1), we show, in Fig. 1, the replication values for different values of  $a_i$  and  $b_i$ . As an application, constants  $a_i$  and  $b_i$  will be estimated in Section 3.2.1 from the experimental data for single infection to determine the replication rates of each strain at the two studied temperatures, thus obtaining the TRN for each PepMV strain.

## 2.2. Dynamical equations for single and mixed infections

The dynamics of virus replication for single infection was modeled using the following one-variable model:

$$f(x_i) = \frac{dx_i}{dt} = r_i(T) x_i \left(1 - \frac{x_i}{K}\right). \quad (2)$$

Here, variable  $x_i > 0$  is the viral load of each strain  $i \in \{E, C\}$ . This equation is the well-known logistic model, here including a  $T$ -dependent replication rate (TRN function given by Eq. (1)). The growth rate is exponential for small population sizes, and the virus populations will grow until the carrying capacity,  $K > 0$  (ng gRNA), is achieved.

The dynamics for mixed infection are modeled similarly to single infection is modeled, while also considering  $T$ -dependent replication rates and including competition between both strains. The strength of the competition by strain  $j$  on strain  $i$  is introduced with (dimensionless) parameters  $\beta_{ij} > 0$ ,  $i, j \in \{E, C\}$ ,  $i \neq j$ . We use the classic Lotka–Volterra competition model, given by the following:

$$\frac{dx_E}{dt} = r_E(T) x_E \left(1 - \frac{x_E + \beta_{EC} x_C}{K}\right), \quad (3)$$

$$\frac{dx_C}{dt} = r_C(T) x_C \left(1 - \frac{\beta_{CE} x_E + x_C}{K}\right), \quad (4)$$

where the two viruses compete for the same cellular resources,  $K$  being the carrying capacity.

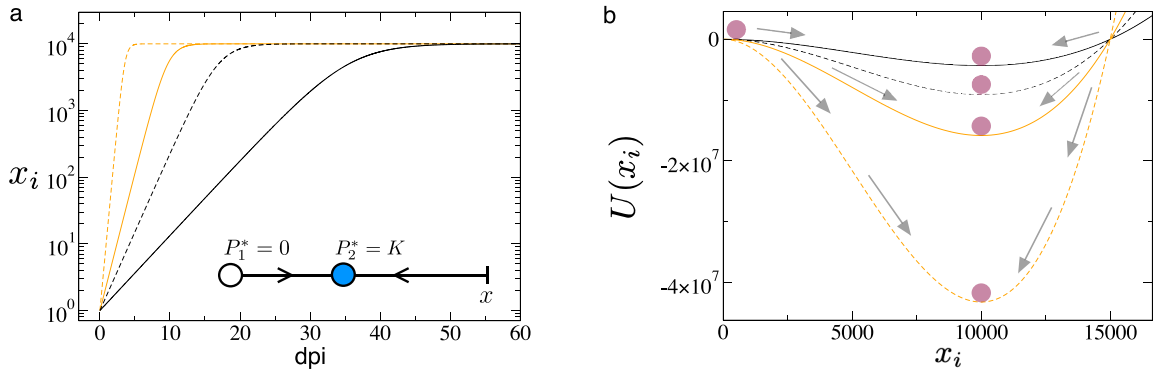


**Fig. 2.** (a) Dynamics (shown in linear-log scale) obtained from Eq. (5) for 60 days post-inoculation (dpi) with  $K = 10^4$ ,  $a_i = 0.2$ , and both  $b_i = 0.01$  (black) and  $b_i = 0.1$  (orange). As the initial conditions, we used  $x_i(0) = 1$ . The solid and dashed lines correspond to temperatures of 20 °C and 30 °C, respectively. The inset displays the phase space of Eq. (2), with two equilibrium points:  $P_1^*$  (white circle) and  $P_2^*$  (blue circle). The arrows indicate the stability of both equilibria. (b) The potential function obtained from Eq. (6) using the same parameter values as used in panel (a) and represented with the same colors and line styles. The local minimum corresponds to the equilibrium point  $P_2^* = K$ , which is stable.

### 3. Results and discussion

In this section, we first discuss the dynamics of the models for both single and mixed infection, focusing on the role of  $T$ -dependent replication. Then, we estimate the parameters describing the TRN of each PepMV strain from single-infection experiments. Finally, we quantify the competition coefficients for both strains from the experimental mixed infection. An overview of the experimental protocols used to characterize the single and double infections with the CH2 and EU strains is provided in Sections A1 and A2 of the Appendix.

#### 3.1. Dynamics

Equation (2) can be solved analytically, giving

$$x_i(t) = \frac{x_i(0) K}{x_i(0) + (K - x_i(0)) \exp(-r_i(T) t)}, \quad (5)$$

where  $x_i(0) > 0$  is the initial conditions and  $t$  is time. Despite being a well-known model, let us summarize the dynamical properties of the logistic model, now considering the  $T$ -dependent replication rate. This system has two equilibrium points, namely  $P_1^* = 0$ , and  $P_2^* = K$ . The stability of this equilibrium is determined from

$$\lambda = \frac{df(x_i)}{dx_i} = r_i(T) \left(1 - \frac{2x_i}{K}\right).$$

It is easy to show that  $P_1^*$  is unstable and  $P_2^*$  is an attractor for  $T_{\min} < T < T_{\max}$  since  $\lambda(P_1^*) = r_i(T) > 0$  and  $\lambda(P_2^*) = -\lambda(P_1^*)$ . That is, for any initial condition, the virus population will always achieve the carrying capacity. Here, the equilibrium values do not depend on  $r_i(T)$  but on how they are approached or left do so. We want to emphasize that the carrying capacity of plant cells might vary depending on the temperature conditions; thus, different equilibria may be achieved at different temperatures (as observed in the experiments). Hence, the values of  $K$  will be estimated from the experiments (see Section B below).

The time dynamics of Eq. (2) can be visualized as shown in Fig. 2(a), by means of time series obtained from the explicit solution given by Eq. (5). The inset in this figure displays a schematic diagram of the phase space, with the equilibria  $P_1^*$  being unstable and  $P_2^*$  being stable. As mentioned,  $T$  has an important effect on the duration of the transients since the eigenvalues are hyperbolic and proportional to  $r_i(T)$ . For the parameter values chosen in Fig. 2(a),  $x_i$  achieves equilibrium faster at 30 °C (dashed lines) than at 20 °C (solid lines). Another way to visualize the dynamics in one-variable dynamical systems is by computing the potential function, here given by

$$U(x_i) = - \int f(x_i) dx_i = r_i(T) x_i^2 \left( \frac{x_i}{3K} - \frac{1}{2} \right). \quad (6)$$

The potential is a cubic polynomial function and appears parabolic in the studied range of  $x_i$  (Fig. 2(b)), with a minimum at the equilibrium value  $P_2^* = K = 10^4$ . Notice that the wells are deeper at 30 °C, meaning that the equilibrium point is much more attracting, in turn explaining why this equilibrium is achieved faster than at 20 °C. However, the dynamics will be slower for  $T$ s above the peak in the TRN (see next section).

We sought to examine competition by studying the dynamics of Eqs. (3)–(4), which have four different equilibrium points, namely  $P_0^* = (0, 0)$ ,  $P_E^* = (K, 0)$ ,  $P_C^* = (0, K)$ , and  $P_{EC}^* = (x_E^*, x_C^*)$ , with

$$x_E^* = \frac{K(\beta_{EC} - 1)}{(\beta_{EC}\beta_{CE} - 1)}, \quad x_C^* = \frac{K(\beta_{CE} - 1)}{(\beta_{EC}\beta_{CE} - 1)}.$$

Note that the fixed points are also independent of the replication rates,  $r_i(T)$ , now also being determined by  $K$  and the competition constants. However, as stated below, the replication rates also play an important role in the transients toward equilibria. The Jacobian matrix reads

$$\mathcal{J} = \begin{pmatrix} r_E(T)(K - 2x_E - x_C\beta_{EC})/K & -r_E(T)x_E\beta_{EC}/K \\ -r_C(T)x_C\beta_{CE}/K & r_C(T)(K - 2x_C - x_E\beta_{CE})/K \end{pmatrix}.$$

The eigenvalues are here given by

$$\lambda_1(P_0^*) = r_E(T), \lambda_2(P_0^*) = r_C(T),$$

and thus  $P_0^*$  is a repeller since  $r_i(T) > 0$ .

The eigenvalues of equilibrium point  $P_E^*$  are

$$\lambda_1(P_E^*) = -r_E(T), \lambda_2(P_E^*) = r_C(T)(1 - \beta_{CE}).$$

Notice that the first eigenvalue is negative (when  $r_E(T) > 0$ ), and the stability of this equilibrium depends on the second eigenvalue. For  $r_E(T) > 0$ ,  $r_C(T) > 0$ , and  $\beta_{CE} > 1$ , the equilibrium  $P_E^*$  is an attractor. For  $r_E(T) > 0$ ,  $r_C(T) > 0$  and  $\beta_{CE} < 1$  the equilibrium  $P_E^*$  is a saddle point. The stability of the equilibrium  $P_C^*$  is similar to the explained above. Here, the eigenvalues are:

$$\lambda_1(P_C^*) = r_E(T)(1 - \beta_{EC}), \lambda_2(P_C^*) = -r_C(T).$$

This equilibrium will be stable when  $\beta_{EC} > 1$  and  $r_E(T) > 0$  and will be a saddle when  $\beta_{EC} < 1$  and  $r_E(T) > 0$  (since the second eigenvalue is always negative). The eigenvalues for equilibrium  $P_{EC}^*$  are

$$\lambda_{\pm}(P_{EC}^*) = \frac{r_E(T)(1 - \beta_{EC}) + r_C(T)(1 - \beta_{CE}) \mp \sqrt{\Delta}}{2(\beta_{EC}\beta_{CE} - 1)},$$

with

$$\Delta = (r_E(T)\Theta + r_C(T)\Gamma)^2 + 4r_E(T)r_C(T)\Theta\Gamma(\beta_{EC}\beta_{CE} - 1), \quad \Theta = \beta_{EC} - 1 \quad \text{and} \quad \Gamma = \beta_{CE} - 1.$$

A global picture of the dynamics is provided in Fig. 3. Panel (a) displays the outcompetition of CH2 by EU, while panel (b) displays the strains' coexistence (as we observed in the experiments performed in this work). Panel (c) provides a bifurcation diagram plotting the equilibrium values of both strains at increasing values of  $\beta_{EC}$ . Notice that for  $\beta_{EC} < 1$ , the two viral strains coexist. At  $\beta_{EC} > 1$ , the coexistence turns into EU being outcompeted by CH2 (see the phase portrait in the inset). The panel below the bifurcation diagram shows the eigenvalues for the fixed points  $P_C^*$  and  $P_{EC}^*$ . Both fixed points collide and interchange stability by means of one eigenvalue through a transcritical bifurcation. Finally, Fig. 4 shows the temporal dynamics, obtained numerically (numerical simulations were performed with a fourth-order Runge–Kutta method with a constant time step  $\Delta t = 0.05$ .) for different temperature values. Here, as shown for the single-infection dynamics, temperatures involving higher replication rates of viral gRNA will allow the equilibrium points to be achieved earlier. However, for temperatures close to the maximum values (e.g., 40 °C and 49 °C) the dynamics slow down again.

### 3.2. Application of the models to the experimental data

In this section, we use the previously described mathematical models to estimate parameters from the experimental data for single and mixed infection with EU and CH2 isolates. Appendix Sections A1 and A2 provide information about the experiments. Further details about experiments can be found in Ref. [50], in which the evolutionary outcomes for both single and mixed infection were studied using next-generation sequencing.

The experimental data processing for the models' fitting is commented on in Section A3. The optimization method used for the fittings, given by a macroevolutionary algorithm (MA), is described in Section A4. The MA is used to compute the parameters providing the best fits after running 50 replicates, as well as the mean values of the optimized parameters and of the best fittings averaged over these replicates.

#### 3.2.1. Single infections

For the single-infection experiment, we used Eq. (2) to estimate the model parameters, considering the vector  $(a_i, b_i, K)$ ,  $i \in \{E, C\}$ , which includes the parameters of the TRN and the plants' carrying capacities. Here, we show the values of the parameters providing the best fit from all 50 replicates of the MA. The mean values ( $\pm SD$ ) of the optimized parameters and of the best parameter sets averaged over the replicates are displayed in supplementary Table SI, together with the best parameter sets, as commented on below.

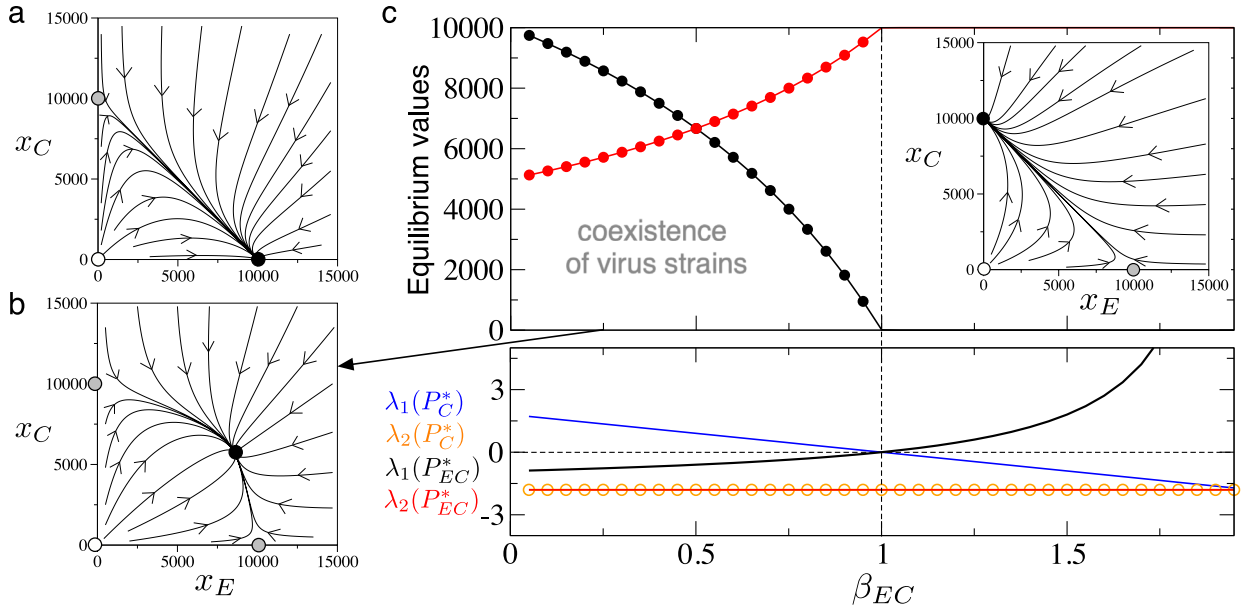


**Fig. 3.** Dynamics of Eqs. (3)-(4). (a) Phase portrait showing the outcompetition of  $x_C$  by  $x_E$ , with  $\beta_{EC} = 0.5$  and  $\beta_{CE} = 1.5$  (the arrows indicate the direction of the orbits; the equilibrium points are shown with solid circles: repeller [white], saddle point [grey], attractor [black]). (b) Coexistence dynamics with  $\beta_{EC} = 0.25$ . Coexistence was observed in the experiments discussed in Section 3.2.2. (c) Bifurcation diagram increasing the competition strength by  $x_C$  on  $x_E$ , computed with  $0.05 \leq \beta_{EC} \leq 1.95$  and  $\beta_{CE} = 0.5$ . Notice that the two strains coexist for  $0 < \beta_{EC} < 1$ . The solid line and the solid dots in black indicate the equilibrium values for  $x_E$  obtained numerically and analytically, respectively. In red, we show the same results for  $x_C$ . At  $\beta_{EC} = 1$ , equilibria  $P_{EC}^*$  and  $P_C^*$  collide in a transcritical bifurcation, and for  $\beta_{EC} > 1$ , the equilibrium  $P_C^*$  becomes the attractor. The lower panel displays the eigenvalues for the fixed points  $P_C^*$  and  $P_{EC}^*$ . In all of the analyses,  $a_E = a_C = 0.8$ ,  $b_E = b_C = 0.02$ ,  $K = 10^4$ , and  $T = 20$  °C.

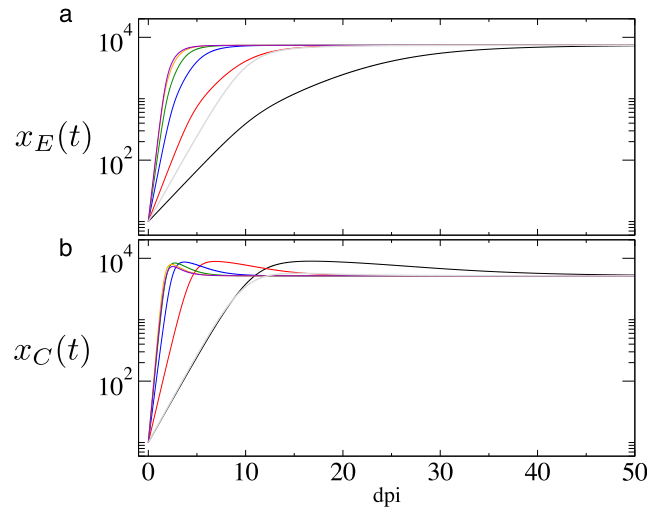


**Fig. 4.** Time dynamics (days post-inoculation [dpi]) in linear-log scale for the viral strains EU ( $x_E(t)$  in panel (a)) and CH2 ( $x_C(t)$  in panel (b)) at different temperatures: 17 °C (black); 20 °C (red); 25 °C (blue); 30 °C (green); 35 °C (orange); 40 °C (violet); and 49 °C (grey). Here, we have used  $a_E = 0.2$ ,  $b_E = 0.1$ ,  $\beta_{CE} = 0.65$ ,  $a_C = 0.4$ ,  $b_C = 0.05$ ,  $\beta_{EC} = 0.5$ , and  $K = 10^4$ .

The parameters providing the best fit for EU at 20 °C were  $a_E = 1.5519$ ,  $b_E = 0.8138$ ,  $r_E = 7.7595$  ng gRNA/day, and  $K = 1.9682 \times 10^6$  nggRNA (black trajectory in Fig. 5a), gRNA being genomic RNA. The parameters providing the best fit for the EU data at 30 °C were  $a_E = 1.2681$ ,  $b_E = 0.3841$ ,  $r_E = 19.0123$  ng gRNA/day, and  $K = 4.115 \times 10^5$  nggRNA (red trajectory in Fig. 5a). Concerning CH2, the parameters providing the best fit at 20 °C were  $a_C = 1.1382$ ,  $b_C = 0.0151$ ,  $r_C = 2.0757$  nggRNA/day, and  $K = 4.110 \times 10^6$  nggRNA. This fitting is displayed in Fig. 5(b) with a black line. The parameters giving the best fit for 30 °C experiments were given by  $a_C = 3.5948$ ,  $b_C = 1.3388$ ,  $r_C = 53.9226$  ng gRNA/day, and  $K = 5.159 \times 10^6$  nggRNA (the fitting using these parameters is displayed in Fig. 5(b) in red). The fittings of the same ex-



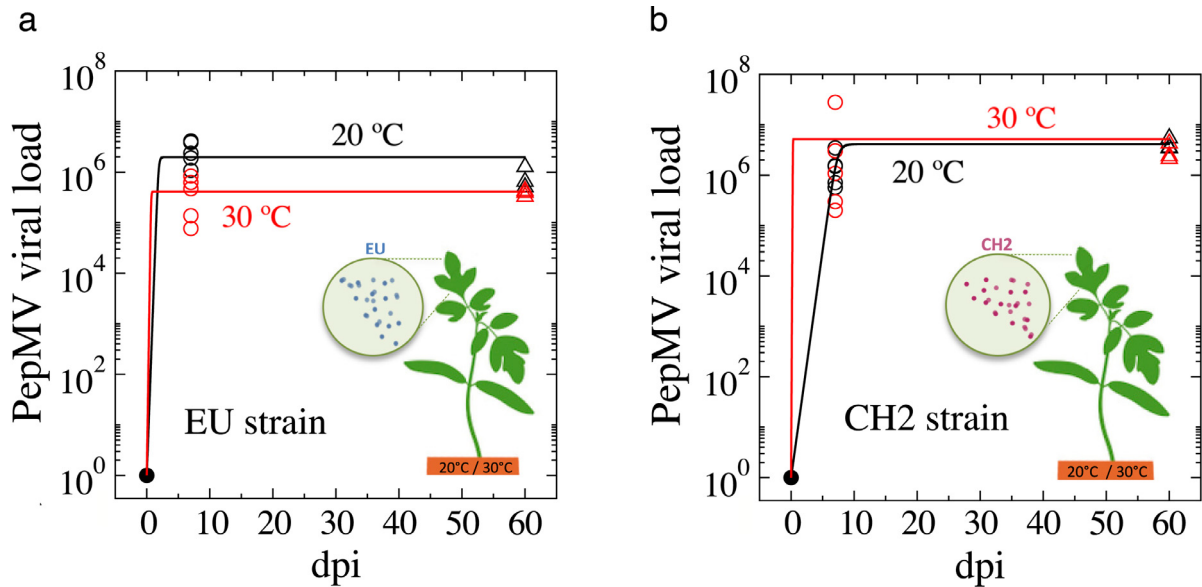


**Fig. 5.** Fitting of the mathematical model to the experimental data using the best vector of parameters obtained from 50 replicates of the macroevolutionary algorithm (MA) for single infection of the EU (a) and CH2 (b) strains. The open circles show experimental data at 20 °C (black) and 30 °C (red); the time trajectories show the dynamics obtained with the mathematical model; and the solid dots show the initial conditions. The fittings were performed using the explicit solution given by Eq. (5).

perimental data above, but obtained from the mean values of the optimized parameters and of the best parameter fits, are shown in supplementary Fig. S1 using the same colors as in Fig. 5. The replication rates for the EU strain appeared to be slightly higher at 30 °C, although the equilibrium value was lower than at 20 °C, indicating a slower initial growth of EU at 20 °C, due to its carrying capacity being larger at this  $T$ . Regarding CH2 dynamics, its carrying capacities were larger than those of EU, with replication rates faster at 30 °C than at 20 °C, as described for EU.

Figure S2 displays how optimization was performed using the MA. Specifically, it shows the evolution of the mean distances,  $\langle d_i \rangle^-$ , along the generations of the MA, computed from the first, i.e., the best  $N/4$  vectors of parameters during the optimization for the EU (panel (a) at 20 °C; panel (b) at 30 °C) and CH2 (panel (c) at 20 °C; panel (d) at 30 °C) strains (Fig. S2). The main panels show the overlapping results for five replicates. The insets display the decrease of the distances for the best vectors of parameters at each improvement event, which are shown overlapped for 25 replicates.

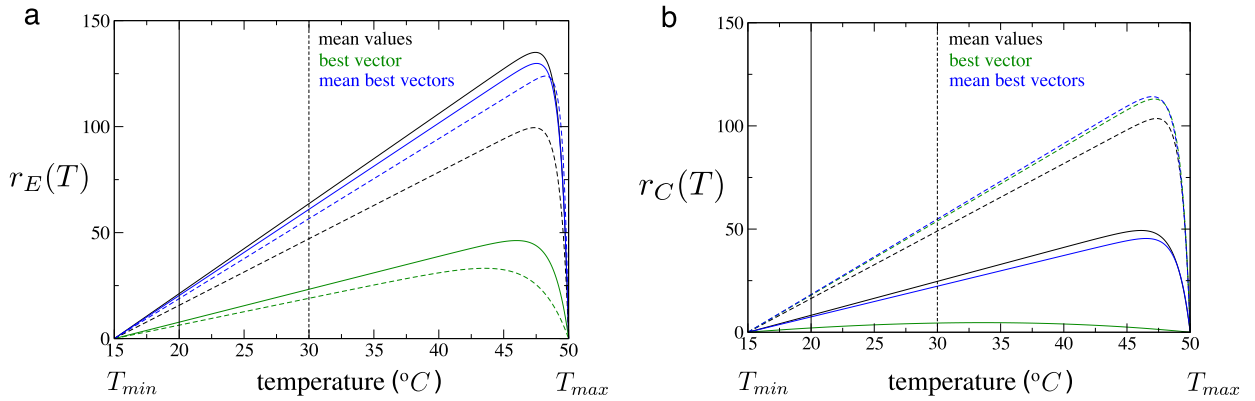
The estimation of parameters  $a_i$  and  $b_i$  from single-infection experiments allows the reconstruction of the TRN for each strain. According to the experimental data and Eq. (1), the replication rates for both strains follow a similar TRN. The increase of replication rates with  $T$  follows a linear behavior until  $T$  gets close to the maximum value, at which point it experiences a sharp decline. These values should be taken with caution since virus replication at high temperatures could vary due to physiological changes in plant cells as well as different enzymatic activities of molecular components that are crucial for gRNA amplification and virus assembly. At intermediate temperatures, the replication values may likely follow this linear fashion.

Fig. 6 displays these results for strains EU (a) and CH2 (b). Each plot shows six predictions: three for the experiments at 20 °C (solid lines) and three for the ones performed at 30 °C (dashed lines). Here the green curves display the profiles obtained from the  $a_i$  and  $b_i$  values for the best vector of parameters obtained from the full 50 replicates of the MA. The black curves have been computed with the mean values of  $a_i$  and  $b_i$  obtained at the end of the MA algorithm and averaged over the 50 replicates. Finally, the blue lines show the profiles for the values of  $a_i$  and  $b_i$  averaged over the best vectors obtained for each replicate of the MA.

Regardless the values of  $a_i$  and  $b_i$  (especially for the best vector of CH2 at 30 °C), the shapes of the estimated TRNs remain similar, meaning that this result, despite the limitations of the experimental data and the selected function,  $r_i(T)$ , remains consistent. Future research may experimentally check whether virus replication falls into this type of TRN and locate the optimal  $T$  value above which virus replication slows down as  $T$  increases.

### 3.2.2. Mixed infections

In the previous section, we estimated the parameter values for the single infections, obtaining the  $T$ -dependent replication rates and the carrying capacities for each viral strain at each studied temperature. The main goal of the experiments with the mixed infections was to characterize the competition between EU and CH2 strains at different temperatures. To do so, we fixed the values of  $r_E(T)$  and  $r_C(T)$  using the constants  $a_E$ ,  $b_E$ , and  $a_C$ ,  $b_C$  which gave the best fits in the single-



**Fig. 6.** Viral thermal reaction norms (TRNs) for each isolate, obtained from the estimated parameters of the experimental data of Section 3.2.1. Curves  $r_E(T)$  for EU (a) and  $r_C(T)$  for CH2 were built from the best parameters (green); from the mean values of the optimized parameters (black) for the 50 replicas of the MA; and from the mean of the best vectors (blue), also computed from the replicas of the MA. The solid and dashed lines show the data for the experiments at 20 °C and 30 °C, respectively.

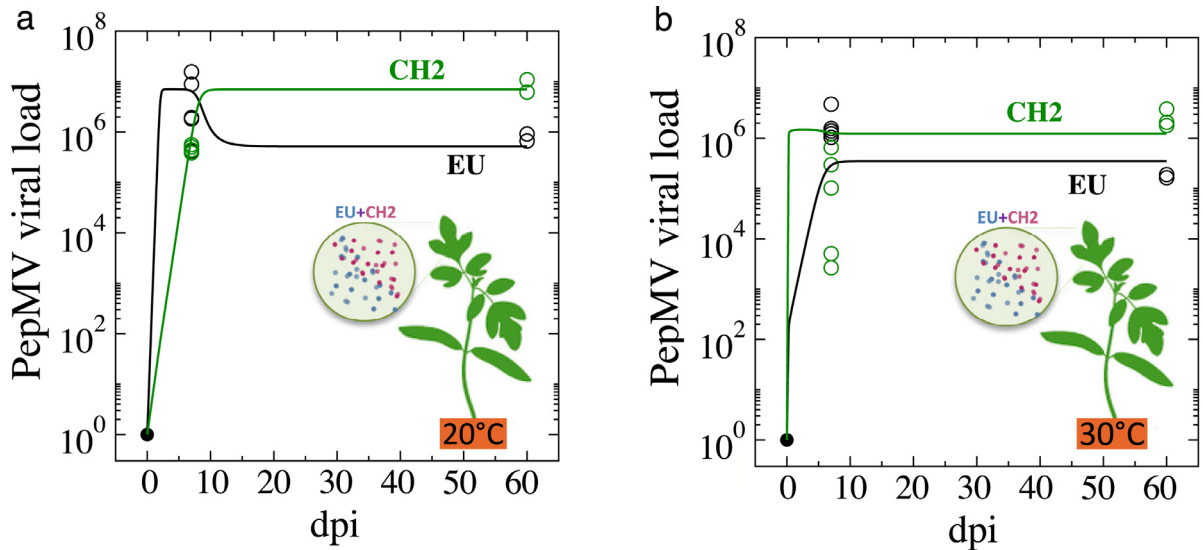


**Fig. 7.** Fitting of the experimental data (open circles) for mixed infections (EU strain [black], CH2 strain [green]) obtained with the mathematical model (solid time series) given by Eqs. (3)–(4) using the parameters obtained with the best fit from 50 replicas of the MA. Panels (a) and (b) display the dynamics of competition at  $T = 20$  °C and  $T = 30$  °C, respectively. The same results for the mean values of the optimized parameters and for the best parameter vectors averaged over the replicates are shown in Fig. S3.

infection experiments. Because the two viral strains were co-infecting the same cells in this experiment, the carrying capacity values estimated in the single-infection might differ. Hence, we will introduce the vector  $(\beta_{EC}, \beta_{CE}, K)$  as free parameters, with  $\beta_{EC}$  and  $\beta_{CE}$  being the competition coefficients among the virus strains. Notably, the competition terms introduced in the mathematical model affect the net replication rate of the viral strains. As mentioned, in order to obtain clear results about the interference due to competition, we used the estimated replication rate of each viral strain at each temperature:  $r_E(T = 20) = 7.7594$ ,  $r_C(T = 20) = 2.0757$ ,  $r_E(T = 30) = 19.0122$ , and  $r_C(T = 30) = 53.9225$ .

The parameter values providing the best fits for the competition experiments performed at 20 °C were  $\beta_{EC} = 0.9319$ ,  $\beta_{CE} = 0.0793$ , and  $K = 7.0418 \times 10^6$ . The results for the experiments at 30 °C were  $\beta_{EC} = 0.9291$ ,  $\beta_{CE} = 0.749$ , and  $K = 1.4967 \times 10^6$ . The mean values obtained for the optimized and best parameter vectors averaged over the 50 replicates are also displayed in Table 1. The time dynamics obtained from the parameters providing the best fits are shown in Fig. 7. While the CH2 strain exerted a stronger competitive effect at the two studied temperatures, the EU had stronger competition at 30 °C than at 20 °C. These results suggest that temperature can greatly modify the competitive interference between these two isolates, resulting in important changes at the levels of within-host transient dynamics and equilibrium values.



**Table 1**  
Parameter values estimated using the MA for the competition experiments at 20 °C and 30 °C using Eqs. (3)–(4). The best parameters displayed in the first three rows of the table were used to fit the experimental data from Fig. 7.

Parameters	Competition at 20 °C	Competition at 30 °C
best $\beta_{EC}$	0.9319	0.9291
best $\beta_{CE}$	0.0793	0.7497
best $K$	$7.0418 \times 10^6$ ng gRNA	$1.4967 \times 10^6$ ng gRNA
$\hat{\beta}_{EC} \pm SD$	$0.9319 \pm 1.8 \times 10^{-7}$	$0.9290 \pm 4.16 \times 10^{-5}$
$\hat{\beta}_{CE} \pm SD$	$0.0793 \pm 5.9 \times 10^{-8}$	$0.7490 \pm 7.37 \times 10^{-4}$
$\hat{K} \pm SD$	$7.0418 \times 10^6 \pm 13.28$ ng gRNA	$1.4949 \times 10^6 \pm 982.47$ ng gRNA
$\langle \text{best} \beta_{EC} \rangle \pm SD$	$0.9318 \pm 1.4 \times 10^{-6}$	$0.9291 \pm 4.17 \times 10^{-5}$
$\langle \text{best} \beta_{CE} \rangle \pm SD$	$0.0793 \pm 4.9 \times 10^{-7}$	$0.7490 \pm 7.38 \times 10^{-4}$
$\langle \text{best} K \rangle \pm SD$	$7.0418 \times 10^6 \pm 60.92$ ng gRNA	$1.4948 \times 10^6 \pm 1050.09$ ng gRNA

4. Conclusions

In this article, we combined mathematical models incorporating temperature-dependent replication rates for viral strains in single and mixed infections with experimental research using two strains of *Pepino mosaic virus* (PepMV): the European (EU) and the Chilean (CH2) strains. The single-infection model allowed us to estimate the relationship between the viral replication and the temperature of growth of the host *i.e.*, the thermal reaction norm of the two strains. Thermal reaction norms of parasites are scarce in the literature, which has largely focused on host species [55]. By means of the two-dimensional Lotka–Volterra model, we explored the dynamics of strain’s competition, together with the *T*-dependent replication. We provided a linear stability analysis of the equilibrium points and identified, as expected, a transcritical bifurcation separating the coexistence phase with out-competition. Then, we used the fitness parameters estimated using data with the single-infection model to quantify the strength of interference at increasing temperatures during mixed infections. Interestingly, the coexistence equilibria were independent of replication rates, instead being determined by the carrying capacity and interference coefficients. However, the linear stability analysis indicated that the (temperature-dependent) replication rates indeed affected the transients. We found that the CH2 strain interfered more strongly at 20 °C. Our models, despite their simplicity, may be useful for future studies relating intrinsic ecological dynamics (such as competition) to changes in *T*, and may be of interest to model mixed virus dynamics under future climatic scenarios.

**Data accessibility.** The raw experimental data can be obtained from Dryad at: <https://datadryad.org/stash/share/xTPRVHo8V1LSFWBJFPZ2USy3pipcsggkCIIlg2vAy6s>.

**Authors’ contributions.** PG conceived of and designed the study; JS and SFE conceived of the mathematical model; JS analyzed the mathematical models and programmed the optimization algorithm; CA performed the experiments; and all of the authors participated in data analysis, wrote the article, and gave final approval for publication.

**Funding.** J.S. has been partially funded by the CERCA Program of the [Generalitat de Catalunya](#), by the Ministry of Economy, Industry and Competitiveness (MINECO) grant MTM2015-71509-C2-1-R, by Agencia Estatal de Investigación (AEI) grant RTI2018-098322-B-I00, and by a Ramón y Cajal contract (RYC-2017-22243). C.A. was funded by the MINECO within a PhD program grant (FPU16/02569). This work was also supported by the AEI-FEDER grants AGL2014-59556-R and AGL2017-89550-R to P.G. and PID2019-103998GB-I00 to S.F.E. The funders had no role in the study design, data collection and analysis, decision to publish, or preparation of the manuscript.

Declaration of Competing Interest

We declare we have no competing interests.

Appendix A

A1. Plant growth conditions, virus inoculation, and sampling

The viral stocks used in all of the experiments were produced as follows. Two infectious PepMV clones belonging to the EU [56] and the CH2 [51,57] strains were used to agroinfiltrate *Nicotiana benthamiana* Domin plants. At 14 days post-inoculation (dpi), viral particles were purified from the homogenized plant tissue, following a series of centrifugations and precipitation [58,59]. Tomato plants (*Solanum lycopersicum* L. cv. Money Maker) were grown in a greenhouse with a photoperiod of 16 h light: 8 h dark and a temperature between 22 °C and 26 °C. At 30 days post-germination, two sets of 33 plants were placed into a greenhouse with temperature conditions of 20 °C or 30 °C. For each temperature, six tomato plants were mock-inoculated, and nine plants per treatment were mechanically inoculated with the EU strain, the CH2 strain, or an equimolar mixture of both strains, *i.e.*, mixed infections. The inoculations were performed on the third and fourth true leaves by rubbing carborundum and a suspension of virions particles at 500 ng/μL in sodium phosphate buffer (30 mM).

PepMV infections were detected by dot-blot molecular hybridization using specific RNA probes to detect the EU and CH2 strains [60].

#### A2. Quantification of virus accumulation

Tomato plants were mechanically inoculated with EU or CH2 strains in single and mixed infections (five plants per treatment). This experiment was carried out twice, in a greenhouse under temperature conditions of 20 °C or 30 °C. At 7 dpi, total RNA was extracted using TRI reagent. Viral RNA accumulation was estimated from samples collected at 7 and 60 dpi by reverse-transcriptase real-time quantitative PCR (RT-qPCR). The copy number of PepMV genomes was calculated from the  $C_T$  values and the molecular weight of PepMV genome per ng of total RNA.

#### A3. Experimental data processing

The experimental data were processed for the fitting and parameter-estimation process. We built time series from the experimental data using the replicates obtained at 7 and 60 dpi for each viral strain, and also included the known initial conditions. That is, for each temperature, we built different time series for single and mixed infections, resulting in eight different data sets (four time series for the single infections plus 4 time series for the mixed ones). Since several replicates were obtained, we applied the optimization algorithm described below to all of the replicates simultaneously. In order to merge all this information into time series, we re-scaled the experimental data since the initial conditions used experimentally at 7 and 60 dpi were different. The data re-scaling was applied to all of the data points (including the initial conditions), using:

$$x_i^s(t) = (x_i(t) - x_i^{(t)}(0)) + 1, i \in \{E, C\}, t \in \{0, 7, 60\},$$

where  $x_i^s(t)$  was the scaled data at time  $t$  and  $x_i^{(t)}(0)$  was the initial conditions used for the experiments performed during time  $t$  ( $x_i^{(t=7)}(0) = 150$  ng gRNA or  $x_i^{(t=60)}(0) = 899$  ng gRNA). By applying this re-scaling, we took into account the net increase of the population starting at the same initial condition, which was set to 1 gRNA, since  $x_i(0) - x_i^{(t)}(0) = 0$ .

#### A4. Macroevoolutionary algorithm

We used a macroevolutionary algorithm (MA) [61] to find the values of the model parameters providing the best fit to the experimental data. This algorithm considered a population of vectors of parameters to which a fitness value was attributed, depending on how well were these sets of parameters fit the mathematical model to the data. This fitness value is usually given by a distance measure between the simulated data (i.e., data obtained from the mathematical model) and the data measured in the experiments (here, we used least-squares; see below). The MA involved selecting the fittest parameters due to evolution and macro-extinction processes. The MA was implemented as follows:

◆ Define a population,  $\Omega(N)$ , with  $N$  vectors of parameters,  $\vec{v}_i^{(k)} = (a_i, b_i, \beta_{ij}, \beta_{ji}, K)^{(k)}$ , with  $i, j \in \{E, C\}$ ,  $i \neq j$ ;  $1 \leq k \leq N$ . Note that for single infections,  $\beta_{ij} = \beta_{ji} = 0$ .

◆ Define exploratory ranges for each parameter. We give the following ranges for the model parameters:  $a_i, b_i \in [10^{-5}, 10]$ ,  $\beta_{ij}, \beta_{ji} \in (0, 1)$ ,  $K \in [10^3, 10^{11}]$ . Because the ranges for parameters  $a_i$  and  $b_i$  include several orders of magnitude, we sampled the exponents from the uniform distribution  $U(-5, 1)$ . The analyses developed for the mixed-infection model (Section 3.1) indicated that the values of  $\beta_{EC}$  and  $\beta_{CE}$  must be positive and lower than 1 to ensure the coexistence of strains, as observed in the competition experiments. Because we are interested in the relative values of  $\beta_{EC}$  and  $\beta_{CE}$ , and due to the dynamical restrictions discussed above, we explored the range (0,1) for both competition coefficients. Finally, the carrying capacity was explored for the range  $10^3 \leq K \leq 10^{11}$ , also sampling the exponents from the uniform distribution  $U(3, 11)$ .

◆ Initialize  $\Omega(N, \tau = 0)$  with random values within the intervals defined above. Once the initial population of  $N$  vectors is initialized, the macroevolutionary generations,  $\tau$ , start. At each generation  $\tau$ , we applied the next rules:

1. For each vector  $\vec{v}_i^{(k)}$ , compute the distance (labeled as  $d_i^{(k)}$ ) between the simulated data,  $x_i^{(k)}(t)$ , obtained with the vector of parameters  $\vec{v}_i^{(k)}$  and the re-scaled experimental data, now labeled as  $\varepsilon(t)$ , by means of the least squares. The simulated solutions for the single infections were computed from the analytical solution given by Eq. (5), while for mixed infections, the solutions were obtained by integrating Eqs. (3)–(4) numerically. Recall that for both single and mixed infections, the initial conditions are  $x_i(0) = 1$ . Because several replicates are available for each time point ( $t_1 = 7$  dpi and  $t_2 = 60$  dpi), we computed a single distance value using the least squares, employing:

$$d_i^{(k)} = \frac{F}{(n_7 + n_{60})} \left( \sum_{j=1}^{n_7} (x_j^{(k)}(t_1) - \varepsilon(t_1))^2 + \sum_{m=1}^{n_{60}} (x_m^{(k)}(t_2) - \varepsilon(t_2))^2 \right),$$

with  $n_7$  and  $n_{60}$  being the number of experimental replicas at 7 and 60 dpi, respectively. Due to the large viral loads measured in the experiments, we multiplied the distances by a factor  $F = 10^{-4}$  to handle lower numbers. This does not affect the parameter-optimization process because it was applied to all of the simulations. For single infections, we computed  $d_i^{(k)}$

for each strain and each studied temperature (20 °C and 30 °C). For mixed infections, we computed the distance, taking into account the amounts of gRNA for the two virus strains simultaneously. For this case, the distance was computed using:

$$D_m^{(k)} = \frac{1}{2} (d_E^{(k)} + d_C^{(k)}). \quad (7)$$

2. Order the whole vectors of the population from shortest to longest distances.
3. Select a 25% of the vectors with the lowest distances (the first  $N/4$  vectors), while removing all others (macroextinctions).
4. Then, initialize the population  $\Omega(N, \tau + 1)$  with the 25% of the survival vectors (following the order from lowest to highest distances). Together with the selected vectors, the population at  $\tau + 1$  will also include the same selected vectors but slightly perturbed. The perturbations consider small variations, i.e.,  $\vec{v}_i^{(k)} = (a_i(1 \pm \mu), b_i(1 \pm \mu), K(1 \pm \mu), \beta_{ij}(1 \pm \mu), \beta_{ji}(1 \pm \mu))^{(k)}$ . Here, we will generally use values of  $\mu$  selected uniformly at each time generation within the ranges  $\mu \in [10^{-12}, 10^{-2}]$ . After doing so, the population  $\Omega(N, \tau + 1)$  will have  $\xi = N/2$  vectors. Then, the extinct population of vectors  $N - \xi$  will be replaced at  $\tau + 1$  by other vectors taking random values within the initially given ranges.
5. Go to 1.

This algorithm involved selecting the best parameters, including massive extinctions and the evolution of the best selected vectors along the iterations of the MA. That is, the parameters underwent evolutionary optimization. In our simulations, we used a population size of  $N = 4000$  vectors of parameters. At the end of each MA simulation, we obtained a population of  $N/4 = 10^3$  optimized vectors of parameters, which were averaged and considered as the best mean values of the estimated parameters. We also recorded the parameter vector providing the best fit along the whole MA. In addition, we computed the mean of the parameters providing the best fit for each replica of the MA algorithm. For each experimental data set, we ran 50 replicates of the MA. Each replicate involved a total exploration of 4000 vectors of parameters (initial population) plus 3000 vectors, which were modified (including those with small random perturbations and those extinct) by iteration of the MA algorithm. For single infections, we ran the MA over  $\tau = 10^7$  generations. This gave a total amount of more than  $1.5 \times 10^{12}$  combinations of explored parameters for each single-infection case. For the mixed infections, which had a higher computational cost due to the numerical computation of the solutions, we used  $\tau = 10^6$  generations. For this case, we explored more than  $1.5 \times 10^{11}$  different parameter combinations for each  $T$  value.

## Supplementary material

Supplementary material associated with this article can be found, in the online version, at [10.1016/j.apm.2021.10.008](https://doi.org/10.1016/j.apm.2021.10.008).

## References

- [1] E.C. Griffiths, A.B. Pedersen, A. Fenton, O.L. Petchey, The nature and consequences of coinfection in humans, *J. Infect.* 63 (3) (2011) 200–206.
- [2] J. Syller, Facilitative and antagonistic interactions between plant viruses in mixed infections, *Mol. Plant Pathol.* 13 (2012) 204–216.
- [3] M. Vurro, B. Bonciani, G. Vannacci, Emerging infectious diseases of crop plants in developing countries: impact on agriculture and socio-economic consequences, *Food Secur.* 2 (2010) 113–132.
- [4] P. Lefevre, D.P. Martin, S.F. Elena, D.N. Shepherd, P. Roumagnac, A. Varsani, Evolution and ecology of plant viruses, *Nat. Rev. Microbiol.* 17 (2019) 632–644.
- [5] S.D. Lawn, AIDS In africa: the impact of coinfections on the pathogenesis of HIV-1 infection, *J. Infect.* 48 (1) (2004) 1–12.
- [6] K. Modjarrad, S.H. Vermund, Effect of treating co-infections on HIV1 viral load: a systematic review, *Lancet Infect. Dis.* 10 (7) (2010). 455–63.
- [7] H. Getahun, C. Gunneberg, R. Granich, P. Nunn, HIV infection-associated tuberculosis: the epidemiology and the response, *Clin. Infect. Dis.* 50 (Suppl 3) (2010) S201–S207.
- [8] M. Kang, K. Hollabaugh, V. Pham, S.L. Koletar, et al., Virologic and serologic outcomes of mono versus dual HBV therapy and characterization of HIV/HBV coinfection in a US cohort, *J. Acquir. Immune Defic. Syndr.* 66 (2) (2014) 172–180.
- [9] HIV outcome sin Hepatitis B virus coinfectd individuals on HAART, H.M. Chun, O. Mesner, C.L. Thio, I. Bebu, et al., Infectious disease clinical research program HIV working group, *J. Acquir. Immune Defic. Syndr.* 66 (2) (2014) 197–205.
- [10] P. Gupta, Hepatitis c virus and HIV type 1 co-infection, *Infect. Dis. Rep.* 5 (Suppl 1) (2013) e7.
- [11] A. Alemu, Y. Shiferaw, Z. Addis, B. Mathewos, W. Birhan, Effect of malaria on HIV/AIDS transmission and progression, *Parasit. Vectors.* 6 (2013) 18.
- [12] C.J. Chu, S.D. Lee, Hepatitis b virus/hepatitis c virus coinfection: epidemiology, clinical features, viral interactions and treatment, *J. Gastroenterol. Hepatol* 23 (4) (2008). 512–20.
- [13] S. Creighton, M. Tenant-Flowers, C.B. Taylor, R. Miller, N. Low, Co-infection with gonorrhoea and chlamydia: how much is there and what does it mean? *Int. J. STD. AIDS.* 14 (2) (2003). 109–13.
- [14] D. Perkins, H. Chong, B. Irvine, J. Domagalski, Genital co-infection with herpes simplex viruses type 1 and 2: comparison of real-time PCR assay and traditional viral isolation methods, *J. Cell. Mol. Med.* 11 (3) (2007). 581–4.
- [15] F. Xu, J.A. Schillinger, M.R. Sternberg, R.E. Johnson, et al., Seroprevalence and coinfection with herpes simplex virus type 1 and type 2 in the united states, 1988–1994, *J. Infect. Dis.* 185 (8) (2002). 1019–24.
- [16] L.J. Allen, M. Langlais, C.J. Phillips, The dynamics of two viral infections in a single host population with applications to hantavirus, *Math. Biosci.* 186 (2) (2003) 191–217.
- [17] K.B. Blyuss, Y.N. Kyrchko, On a basic model of a two-disease epidemic, *Appl. Math. Comput.* 160 (1) (2005) 177–187.
- [18] M. Martcheva, S. Pilyugin, The role of coinfection in multidisease dynamics, *SIAM J. Appl. Math.* 66 (3) (2006) 843–872.
- [19] M.J. Keeling, P. Rohani, *Modeling Infectious Diseases in Humans and Animals*, Princeton University Press, Princeton, 2008.
- [20] M.M. Tanaka, M.W. Feldman, Theoretical considerations of cross-immunity, recombination and the evolution of new parasitic strains, *J. Theor. Biol.* 198 (2) (1999) 145–163.
- [21] M. Choisy, J.C. de Roode, Mixed infections and the evolution of virulence: effects of resource competition, parasite plasticity, and impaired host immunity, *Am. Nat.* 175 (5) (2010) E105–E118.
- [22] S. Alizon, Co-infection and super-infection models in evolutionary epidemiology, *Interface Focus* 3 (6) (2013) 20130031.
- [23] S. Alizon, Parasite co-transmission and the evolutionary epidemiology of virulence, *Evolution* 67 (4) (2013) 92–933.

- [24] X. Zhang, K. Cao, The impact of coinfections and their simultaneous transmission on antigenic diversity and epidemic cycling of infectious diseases, *BioMed. Res. Int.* 2014 (2014) 375862.
- [25] T.C. Porco, P.M. Small, S.M. Blower, Amplification dynamics: predicting the effect of HIV on tuberculosis outbreaks, *J. Acquir. Immune. Defic. Syndr.* 28 (5) (2001) 437–444.
- [26] O. Sharomi, C. Podder, A. Gumel, B. Song, Mathematical analysis of the transmission dynamics of HIV/TB coinfection in the presence of treatment, *Math. Biosci. Eng.* 5 (1) (2008) 145–174.
- [27] C.P. Bhunu, W. Garira, Z. Mukandavire, Modeling HIV/AIDS and tuberculosis coinfection, *Bull. Math. Biol.* 71 (7) (2009) 1745–1780.
- [28] L. Roeger, Z. Feng, C. Castillo-Chavez, Modeling TB and HIV co-infections, *Math. Biosci. Eng.* 6 (4) (2009) 815–837.
- [29] A. Nurtay, M.G. Hennessy, J. Sardanyés, L. Alsedà, S.F. Elena, Theoretical conditions for the coexistence of viral strains with differences in phenotypic traits: a bifurcation analysis, *R. Soc. open sci.* 6 (1) (2019) 181179.
- [30] A. Nurtay, M.G. Hennessy, L. Alsedà, S.F. Elena, J. Sardanyés, Host-virus evolutionary dynamics with specialist and generalist infection strategies: bifurcations, bistability, and chaos, *Chaos* 30 (5) (2020) 053128.
- [31] J. Syller, A. Grupa, Antagonistic within-host interactions between plant viruses: molecular basis and impact on viral and host fitness, *Mol. Plant Pathol.* 17 (2016) 769–782.
- [32] A.B. Moreno, J.J. López-Moya, When viruses play team sports: mixed infections in plants, *Phytopathology* 110 (2020) 29–48.
- [33] C. Alcaide, M.P. Rabadán, M.G. Moreno-Pérez, P. Gómez, Implications of mixed viral infections on plant disease ecology and evolution, *Adv. Virus Res.* 106 (2020) 145–169.
- [34] C. Tollenaere, H. Susi, A.L. Laine, Evolutionary and epidemiological implications of multiple infection in plants, *Trends Plant Sci* 21 (2016) 80–90.
- [35] A.F. Read, L.H. Taylor, The ecology of genetically diverse infections, *Science* 292 (2001) 1099–1102.
- [36] D.J. Hodgson, R.B. Hitchman, A.J. Vanbergen, R.S. Hails, R.D. Possee, J.S. Cory, Host ecology determines the relative fitness of virus genotypes in mixed-genotype nucleopolyhedrovirus infections, *J. Evol. Biol.* 17 (2004) 1018–1025.
- [37] J.C. de Roode, R. Pansini, S.J. Cheesman, M.E. Helinski, et al., Virulence and competitive ability in genetically diverse malaria infections, *Proc. Natl. Acad. Sci. U.S.A.* 102 (2005) 7624–7628.
- [38] E. Moriones, J. Navas-Castillo, Tomato yellow leaf curl virus, an emerging virus complex causing epidemics worldwide, *Virus. Res.* 71 (2000) 123–134.
- [39] D. Fargette, A. Pinel-Galzi, D. Sérémé, S. Lacombe, et al., Diversification of rice yellow mottle virus and related viruses spans the history of agriculture from the neolithic to the present, *PLOS Pathog* 4 (2008) e1000125.
- [40] J.P. Legg, P. Lava Kumar, T. Makesh Kumar, L. Tripathi, et al., Cassava virus diseases: biology, epidemiology, and management, *Adv. Virus Res.* 91 (2015) 85–142.
- [41] R. González, A. Butković, S.F. Elena, Role of host genetic diversity for susceptibility-to-infection in the evolution of virulence of a plant virus, *Virus Evol.* 5 (2019) 1–12.
- [42] P.K. Anderson, A.A. Cunningham, N.G. Patel, F.J. Morales, et al., Emerging infectious diseases of plants: pathogen pollution, climate change and agrotechnology drivers, *Trends Ecol. Evol.* 19 (2004) 535–544.
- [43] S.F. Elena, A. Fraile, F. García-Arenal, Chapter 3: Evolution and emergence of plant viruses, in: K. Maramorosch, F.A. Murphy (Eds.), *Adv. Virus Res.*, Academic Press, 2014, pp. 161–191.
- [44] M.R. Rojas, R.L. Gilbertson, Emerging plant viruses: a diversity of mechanisms and opportunities, in: M.J. Roossinck (Ed.), *Plant Virus Evolution*, Springer Berlin Heidelberg, 2008, pp. 27–51.
- [45] J.R. Rohr, J.M. Cohen, Understanding how temperature shifts could map infectious diseases, *PLoS Biol.* 18 (11) (2020) e3000938.
- [46] R.A.C. Jones, Future scenarios for plant virus pathogens as climate change progresses, *Adv. Virus Res.* 95 (2016) 87–147.
- [47] T. Canto, M.A. Aranda, A. Fereres, Climate change effects on physiology and population processes of hosts and vectors that influence the spread of hemipteran-borne plant viruses, *Glob. Chang. Biol.* 15 (2009) 1884–1894.
- [48] P. Trebicki, Climate change and plant virus epidemiology, *Virus Res.* 286 (2020) 198059.
- [49] S. Gupta, N. Ferguson, R. Anderson, Chaos, persistence, and evolution of strain structure in antigenically diverse infectious agents, *Science* 280 (5365) (1998) 912–915.
- [50] C. Alcaide, J. Sardanyés, S.F. Elena, P. Gómez, Increasing temperature alters the within-host competition of viral strains and influences virus genetic variability, *Virus Evolution* 7 (1) (2021) veab017.
- [51] P. Gómez, R.N. Sempere, S.F. Elena, M.A. Aranda, Mixed infections of Pepino mosaic virus strains modulate the evolutionary dynamics of this emergent virus, *J. virol* 83 (2009) 12378–12387.
- [52] D.A. Ratkowsky, J. Olley, T.A. McMeekin, A. Ball, Relationship between temperature and growth rate of bacterial cultures, *J. Bacteriol.* 149 (1982) 1–5.
- [53] D.A. Ratkowsky, R.K. Lowry, A.N. Stokes, R.E. Chandler, Model for bacterial culture growth rate throughout the entire biokinetic temperature range, *J. Bacteriol.* 154 (3) (1983) 1222–1226.
- [54] E. Van Derlinden, J.F. Van Impe, Modeling growth rates as a function of temperature: model performance evaluation with focus on the suboptimal temperature range, *Int. J. Food Microbiol.* 158 (2012) 73–78.
- [55] A.I. Dell, S. Pawar, S.M. Savage, Systemic variation in the temperature dependence of physiological and ecological traits, *Proc Natl Acad Sci U S A* 108 (26) (2011). 10591–6.
- [56] J.M. Aguilar, M.D. Hernández-Gallardo, J.L. Cenis, A. Lacasa, M.A. Aranda, Complete sequence of the Pepino mosaic virus RNA genome, *Arch. Virol.* 147 (2002) 2009–2015.
- [57] R.N. Sempere, P. Gómez, V. Truniger, M.A. Aranda, Development of expression vectors based on pepino mosaic virus, *Plant Meth.* 7 (2011) 6.
- [58] M.G. Abou Haidar, H. Xu, K.L. Hefferon, Potexvirus isolation and RNA extraction, in: G.D. Foster, S.C. Taylor (Eds.), *Plant Virology Protocols: From Virus Isolation to Transgenic Resistance*, Humana Press, Totowa, NJ, 1998, pp. 131–143.
- [59] X. Agirrezabala, E. Méndez-López, G. Lasso, M.A. Sánchez-Pina, M. Aranda, M. Valle, The near-atomic cryoEM structure of a flexible filamentous plant virus shows homology of its coat protein with nucleoproteins of animal viruses, *Elife* 4 (2015) e11795.
- [60] C. Gómez-Aix, C. Alcaide, P. Gómez, M.A. Aranda, M.A. Sánchez-Pina, In situ hybridization for the localization of two pepino mosaic virus isolates in mixed infections, *J. Virol. Methods* 267 (2019) 42–47.
- [61] J. Marín, R.V. Solé, Macroevolutionary algorithms: a new optimization method on fitness landscapes, *IEEE Trans. Evol. Comput.* 3 (4) (1999) 272–286.